D3.4 | X-ray detector
Authors: Zhuoran Geng, Ari Helenius, Ilari Maasilta
Delivery date: 28.02.2023
Version: 1.0

This project has received funding from the European Union's Horizon 2020 research and innovation programme under grant agreement No 800923.

Project Acronym:	SUPERTED
Project Full Title:	Thermoelectric detector based on superconductor-ferromagnet heterostructures
Call:	H2020-FETOPEN-2016-2017
Topic:	FETOPEN-01-2016-2017
Type of Action:	RIA
Grant Number:	800923
Project URL:	https://superted-project.eu/

Editor:	Zhuoran Geng, University of Jyväskylä, JYU Ari Helenius, University of Jyväskylä, JYU Ilari Maasilta, University of Jyväskylä, JYU
Deliverable nature:	Report (R)
Dissemination level:	Public (PU)
Contractual Delivery Date:	28.02.2023
Actual Delivery Date:	28.02.2023
Number of pages:	17
Keywords:	Superconducting thermoelectric detector, ferromagnetic insulator- superconductor heterostructures, tunneling spectroscopy, spin-splitting
Author(s):	Zhuoran Geng, University of Jyväskylä, JYU Ari Helenius, University of Jyväskylä, JYU Ilari Maasilta, University of Jyväskylä, JYU
Contributor(s):	Sanna Rauhamäki, University of Jyväskylä, JYU Tero Heikkilä, University of Jyväskylä, JYU
External contributor(s):	

Abstract

This Deliverable 3.4 *X-ray detector* is a summary of the results of the project for realizing and demonstrating the X-ray detector experimentally. We report here the measurement results from our cryogenic experiments with 22 devices. These results have been used to optimize and improve the design and fabrication protocol of the detector, as well as the design and implementation of the read-out and the measurement setup. One preliminary X-ray detection test is also reported, showing detection of individual X-ray quanta. However, the particular device used was not optimized yet, as it lacked the EuS layer and required an external bias.

This project has received funding from the European Union's Horizon 2020 research and innovation programme under grant agreement No 800923.

1 Introduction

The main task in work package three is to realize and characterize superconductor/ferromagnetic insulator (S/FI) based thermoelectric detector (SFTED) as a microcalorimeter for X-ray detection. In previous deliverables, the schemes of the read-out system and the estimation of the performance of the detector were summarized in D3.1, the implementation of the read-out system and the cryogenic apparatus, and the measured performance of the read-out system were summarized in D3.2, and the detector (chip device) design and fabrication protocols were summarized in D2.2. In this deliverable, we present the results of the experimental work. These results include mainly the characterizations of SFTED devices and the tests of X-ray detection. In addition, we will also present the efforts to optimize and improve the design and fabrication of the device and the modifications on the measurement apparatus beyond what was presented in the earlier deliverables.

In Section 2, we briefly summarize the samples that have been delivered to the University of Jyväskylä (JYU) and the experiments that have been carried out. In Section 3, we present the current-voltage characterization (IVc) of the SFTED devices performed at JYU, reporting our joint effort with CSIC to optimize the device for X-ray microcalorimeter applications. In Section 4, we show the results of our modifications on the detector fabrication (heavy-metal absorber) and the most recent measurement setup. In Section 5, the test results of X-ray detection are demonstrated.

2 Overview of experimental work for the X-ray detector

In this project, JYU is closely collaborating with CSIC to develop the prototype detector device. The S/FI heterostructure junctions are grown by CSIC, and JYU is in charge of re-defining the tunnel junction and depositing a heavy-metal absorber, and then experimentally demonstrating the X-ray detection. There are in total 22 devices that have been processed and measured at JYU, 19 of them were delivered from CSIC, two of them were provided by the external collaborator from MIT, and one normal metal-insulator-superconducting (NIS) junction device was designed and fabricated on-site in JYU for the system testing purposes. All the mentioned devices are listed in Table 1 with descriptions on their compositions and status.

We have carried out a total of 47 successful cryogenic measurements for the SuperTED project. Among these measurements, 26 were conducted to characterize the devices listed in Table 1, 6 were conducted for X-ray detection tests, and 15 measurements were performed for system testing and characterization. A large amount of data has been collected during the project, and we present only a small portion of it here, serving the discussion objectives of this deliverable.

This project has received funding from the European Union's Horizon 2020 research and innovation programme under grant agreement No 800923.

Device	Composition	Arrival Date	Status[a]
SF2101	EuS/Al/AlOx/Co/CaF	Nov.2021	Broken
SF2102	EuS/Al/AlOx/Co/CaF	Nov.2021	Broken
SF2103	EuS/Al/AlOx/Co/CaF	Nov.2021	Broken
SF2104	EuS/Al/AlOx/Co/CaF	Dec.2021	Fine
SF2205	Al/EuS/Cu/CaF	Mar.2022	No junction
SF2206 (two samples from MIT)	Al/EuS/Cu	Jun.2022	No junction
SF2207	Al/EuS/Cu	Jun.2022	Fine
SF2208_dev1	Al/AlOx/Co/CaF	Aug.2022	Broken
SF2208_dev2	Al/AlOx/Co/CaF	Aug.2022	Fine
SF2208_dev3	Al/AlOx/Co/CaF	Aug.2022	Fine
NIS2201 (Made in JYU)	Al/AlOx/Ti/Au	Aug.2022	Fine
SF2209_dev1	Al/AlOx/Co/PMMA	Sept.2022	Fine
SF2209_dev2	Al/AlOx/Co/PMMA	Sept.2022	Fine
SF2209_dev3	Al/AlOx/Co/PMMA	Sept.2022	Fine
SF2210_dev1	EuS/Al/AlOx/Co/PMMA	Oct.2022	Broken
SF2210_dev2	EuS/Al/AlOx/Co/PMMA	Oct.2022	No Junction
SF2210_dev3	Al/AlOx/Co/CaF	Oct.2022	Fine
SF2211_dev1	EuS/Al/AlOx/Co/PMMA	Dec.2022	Fine
SF2211_dev2	EuS/Al/AlOx/Co/PMMA	Dec.2022	In queue
SF2211_dev3	EuS/Al/AlOx/Co/PMMA	Dec.2022	Fine
SF2211_dev4	EuS/Al/AlOx/Co/PMMA	Dec.2022	In queue

Table 1: List of devices measured at JYU

[a]The status "Fine" indicates the device still works, can be measured or processed; "Broken" indicates the device failed during fabrication or measurement; "No junction" indicates the device failed before any measurement or processing; "In queue" indicates the device is not yet processed, and will be measured or processed later.

This project has received funding from the European Union's Horizon 2020 research and innovation programme under grant agreement No 800923.

3 Device characterization and optimization

The working principle of the SFTED has been discussed in detail in several publications [1, 2, 3]. Those studies show that the properties of the tunnel junction significantly determine the performance of the X-ray detection. As mentioned previously, our task is to realize and demonstrate such a device in the X-ray detection tests, therefore, the properties of the devices become the inherently critical information for guiding the design of the detector, read-out scheme, and the cryogenic system.

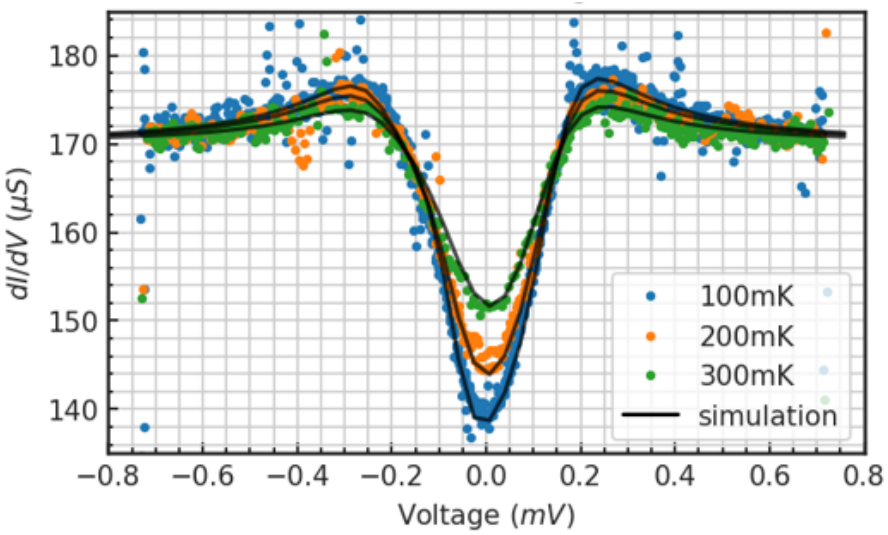

Figure 1: Measured dynamic conductance (dI/dV) of the device SF2103 (points) at three different temperatures with theoretical fits (lines).

The current-voltage characteristics (IVc) of all the S/FI junction samples received from CSIS have been measured at sub-Kelvin temperatures. In Fig. 1 we demonstrate a typical dynamic conductance (dI/dV) of a device (SF2103, see Table 1 for the full list of devices) at three different bath temperatures. These results were numerically fitted to the theory[4, 5], and the key parameters of the tunnel junction were thereby extracted. Table 2 lists these key parameters, and an example of the fitting results for the device shown in Fig. 1.

Parameter	Result
Tunnel resistance R_T	5.9 kΩ
Energy gap Δ_0	0.22 meV
Broadening parameter Γ	$0.3\Delta_0$
Exchange field h	$0.4\Delta_0$
Polarization P	0.43

Table 2: Fitted parameters of the SF2103 device.

Among these parameters, the superconducting energy gap Δ_0, the exchange field h and the polarization P have little variance among all the samples measured, whereas, with the efforts by CSIC, the broadening parameter Γ has been improved to a lower value of $\Gamma = 0.04 \sim 0.07\Delta_0$ in recent samples, as listed in Table 3.

It has been shown in Refs. [1, 3] as well as in deliverable D3.1 that the value of the tunneling resistance R_T of the S/FI junction is critical to the performance of the SFTED as an X-ray detector. In particular, with a current-amplified read-out scheme proposed in this project, $R_T < 100\ \Omega$ is preferred because then the detector output current is higher, matching better

This project has received funding from the European Union's Horizon 2020 research and innovation programme under grant agreement No 800923.

Device	R_T (kΩ)	Γ (Δ_0)
SF2208_dev1	15.4	0.07
SF2208_dev2	60	0.06
SF2208_dev3	6.5	0.05
SF2209_dev1	4.8	0.04
SF2209_dev2	8.2	0.05
SF2209_dev3	7.7	0.06

Table 3: Fitted tunnel resistance and broadening parameters of devices SF2208 and SF2209.

to the read-out SQUID amplifier noise. The influence of R_T on the estimated energy resolution of the detector is demonstrated in Fig. 2 (a), where the optimal low energy resolution region lies at around $T = 0.2$ K and $R_T < 100$ Ω.

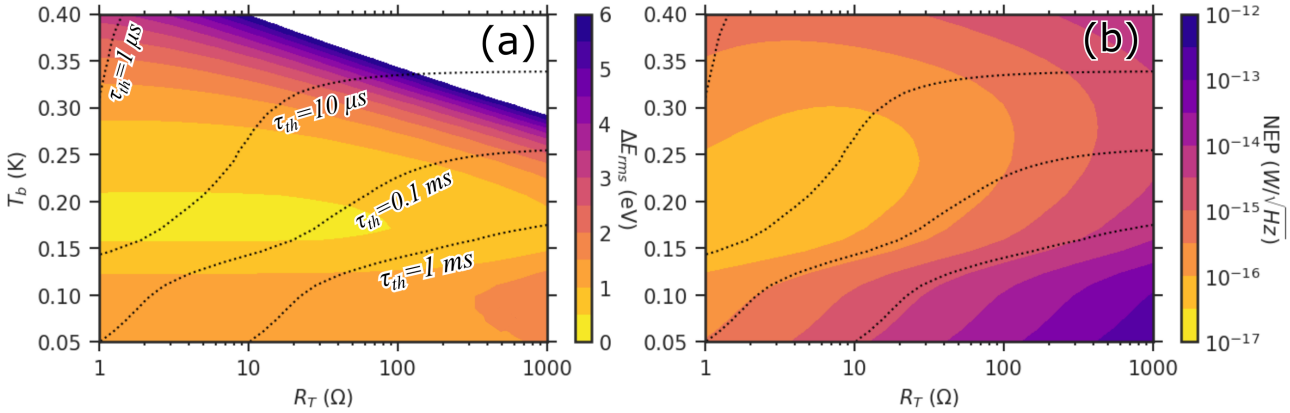

Figure 2: Color scaled theoretically estimated detector energy resolution ΔE as a function of bath temperature T_b and tunnel resistance R_T (a) without the read-out noise. (b) The total low-frequency noise equivalent power (NEP) at 100 kHz, including the SQUID read-out noise. The black dotted lines show values of constant detector pulse fall times.

At the early stages of the project, the S/FI junction samples fabricated by CSIC routinely had $R_T > 5$ kΩ, orders of magnitude higher than the targeted value, thereby failing to satisfy the requirement as an X-ray detector. With a close collaboration with CSIC, a series of 10 cryo-measurements were carried out for three batches and a total of seven test samples, to optimize the fabrication process at CSIC and to lower the R_T of the sample. These test samples consisted of Al/AlOx/Co layers without the bottom EuS layer, and the insulating barrier was produced by oxidizing the Al wire by plasma oxidation the same way as for the samples with an EuS layer. By changing the oxidation time, the barrier thickness can be adjusted, leading to tuning of the junction resistance, as presented in Fig. 3.

In the left panel of Fig. 3, the dynamic conductance of the test samples, measured at ∼ 0.3 K, are demonstrated. In addition to the fact that R_Ts can be extracted from the large-bias asymptote of the measured dynamic conductance, these results also show that the change of the oxidation time does not change the general shape of the current-voltage characteristics of the tunnel junction. In other words, increasing the junction transparency does not seem to greatly affect the subgap density of states. Hence it seems that the subgap density of states is not due to pinholes in the junction. The extracted R_T values are plotted as a function of the oxidation time as blue dots in the right panel. We find that the sample with 1 hour oxidation time provides $R_T = 100$ Ω, thus satisfying the requirement for the X-ray detector.

Based on this optimization work, the more recently fabricated detector samples (including EuS layers) with shorter 1-2 hour oxidation times were measured to have reasonable R_T, as

This project has received funding from the European Union's Horizon 2020 research and innovation programme under grant agreement No 800923.

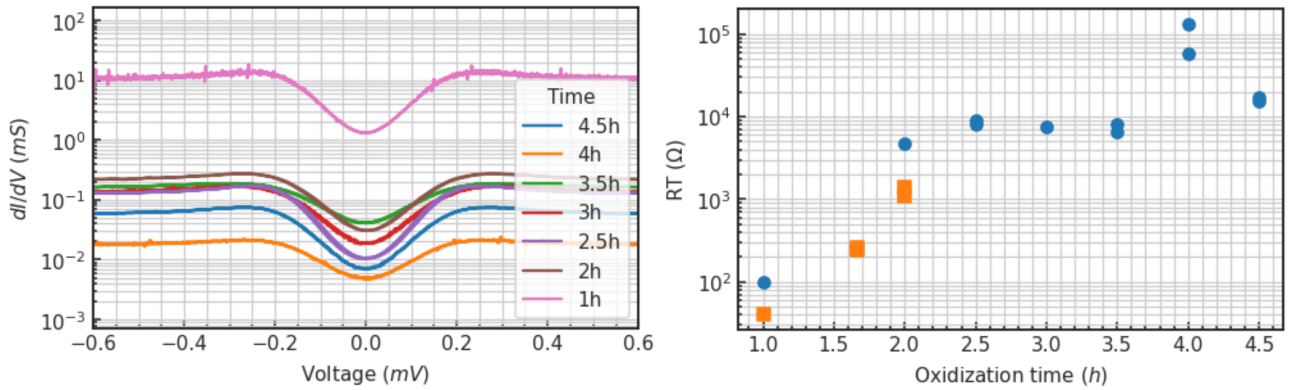

Figure 3: Left panel shows the measured dynamic conductance of Al/AlOx/Co junctions with different plasma oxidization times (colored lines). Right panel shows the R_T as function of the oxidization time. The blue dots are the extracted large-bias dynamic conductance values extracted from a cryo-measurement using the test samples, the orange squares are the measured room temperature junction resistance values from samples prepared for detectors.

shown by the orange squares in the right panel of Fig. 3.

This project has received funding from the European Union's Horizon 2020 research and innovation programme under grant agreement No 800923.

4 Modifications on detector fabrication and measurement setup

Based on the properties characterized from the delivered samples and the practical challenges discovered from the experiments, we have optimized and improved the detector fabrication and the experimental setup with multiple iterations.

4.1 Device fabrication protocol

The X-ray detector fabrication protocol reported in D2.2 has been modified. We found that the tunnel junction can be damaged by the discharge over the surface of the device during argon plasma sputtering process, which was carried out to remove the native oxide layer on the aluminum wire. Therefore, a chemical etching process using 1.25% tetramethylammonium hydroxide (TMAH) water solution was tested and adopted into our fabrication protocol. The updated chemical etching recipe is:

1. Mask layer: PMMA 950, 600 nm, bake at 160 ° C
2. E-beam patterning: 20 kV, 30 μm aperture, 215 $\mu C/cm^2$ area dose
3. Development: 40 sec in IPA:MIBK, 1 min IPA rinse
4. Wet etching: Dip device in 1.25% TMAH water solution for 4 s, rinse with DI-water and keep the device in water before deposition.

We should emphasize that the device should be kept "wet", e.g. covered with water film without blowing it dry, until it has been transferred to the vacuum chamber for metal deposition. Following such a protocol, the water film can prevent the oxidation of the Al wire for a short period ($\sim$ minutes). This new process is safe to the junction, easily executed, and does not require advanced instrumentation such as an in-situ Ar plasma sputtering gun inside the evaporation chamber. It is therefore considered to be a good improvement over the originally proposed recipe. In Fig. 4 we demonstrate a complete detector fabricated via the latest protocol.

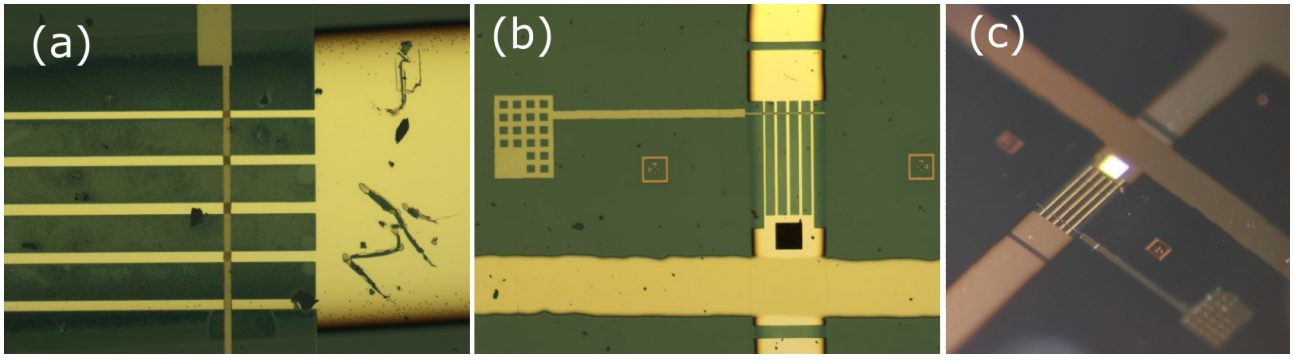

Figure 4: (a) Nb-Al contacts after using the TMAH chemical etching recipe. (b) and (c) show the optical microscope image of a complete detector fabricated via the latest protocol.

4.2 Magnetic coil

In deliverable D3.2 we presented our design of an on-stage superconducting coil [see Fig. 5 (a)], which is required to be used to magnetize the EuS layer of SFTED at temperature below its Curie temperature before X-ray detection test. Such coil was implemented as shown in the

This project has received funding from the European Union's Horizon 2020 research and innovation programme under grant agreement No 800923.

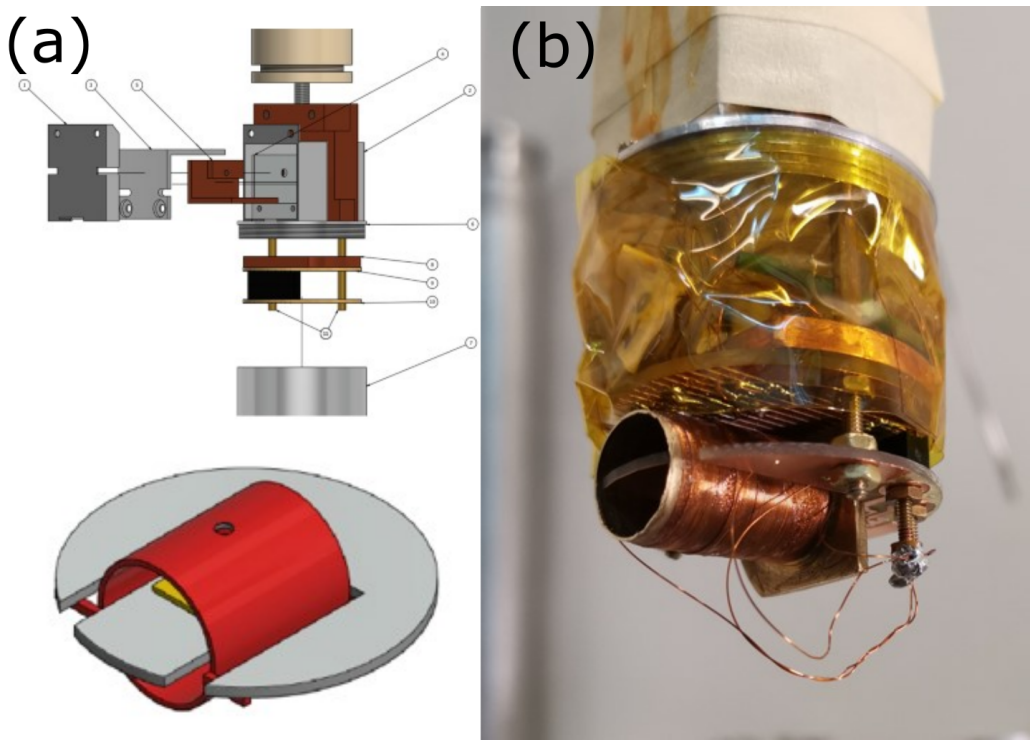

Figure 5: The abandoned superconducting coil implementation. (a) The coil design proposed in report D3.2. (b) The implementation of the design, which was abandoned due to the extra heat load.

panel (b) of Fig. 5, and was capable of producing maximum of ±22 mT fields in the in-plane direction of the device. However, a large part of the wiring of the coil was inside the vacuum chamber, thermalized to a temperature much lower than the helium (He) bath. As a result, significant heat load was applied to the low temperature stage when the magnetic field was fired up, constantly disrupting the experiment.

After several rounds of trial-and-error efforts, we replaced the on-stage coil to one that is mounted outside of the vacuum chamber, directly thermalized with the liquid He bath, as shown in Fig. 6 (a). Such implementation is not only to avoid the additional heat load to the low temperature setup, but also allows a higher maximum field of ±120 mT to be applied to the device, close to an order of magnitude improvement over the original implementation.

To adapt the change of the superconducting coil, the sample stage was also adjusted from horizontal to vertical orientation inside the vacuum chamber, as demonstrated in panel (b) of Fig. 6. This is because the direction of the magnetic field produced by the new coil implementation is changed to align with the central line of the cylindrical vacuum chamber. In addition, the superconducting shielding over the sample stage has been replaced by a Cu cover(not shown) to allow the applied magnetic field to pass through.

4.3 X-ray source and mount

Two Fe-55 (VZ-2878-model) radiation sources were obtained, and were calibrated on Nov.2021 having activities of 156 kBq (thousand counts per second) and 316 MBq, respectively, producing X-rays through the decay of Fe-55 by electron capture into Mn-55, dominantly at an energy of 5.899 keV (K-α). The lower activity source (156 kBq) is intended to be used for characterizing the device and providing proof of concept measurements of the SFTED (easier analysis because of well separated pulses), whereas the higher activity source (316 MBq) is planned for the studies

This project has received funding from the European Union's Horizon 2020 research and innovation programme under grant agreement No 800923.

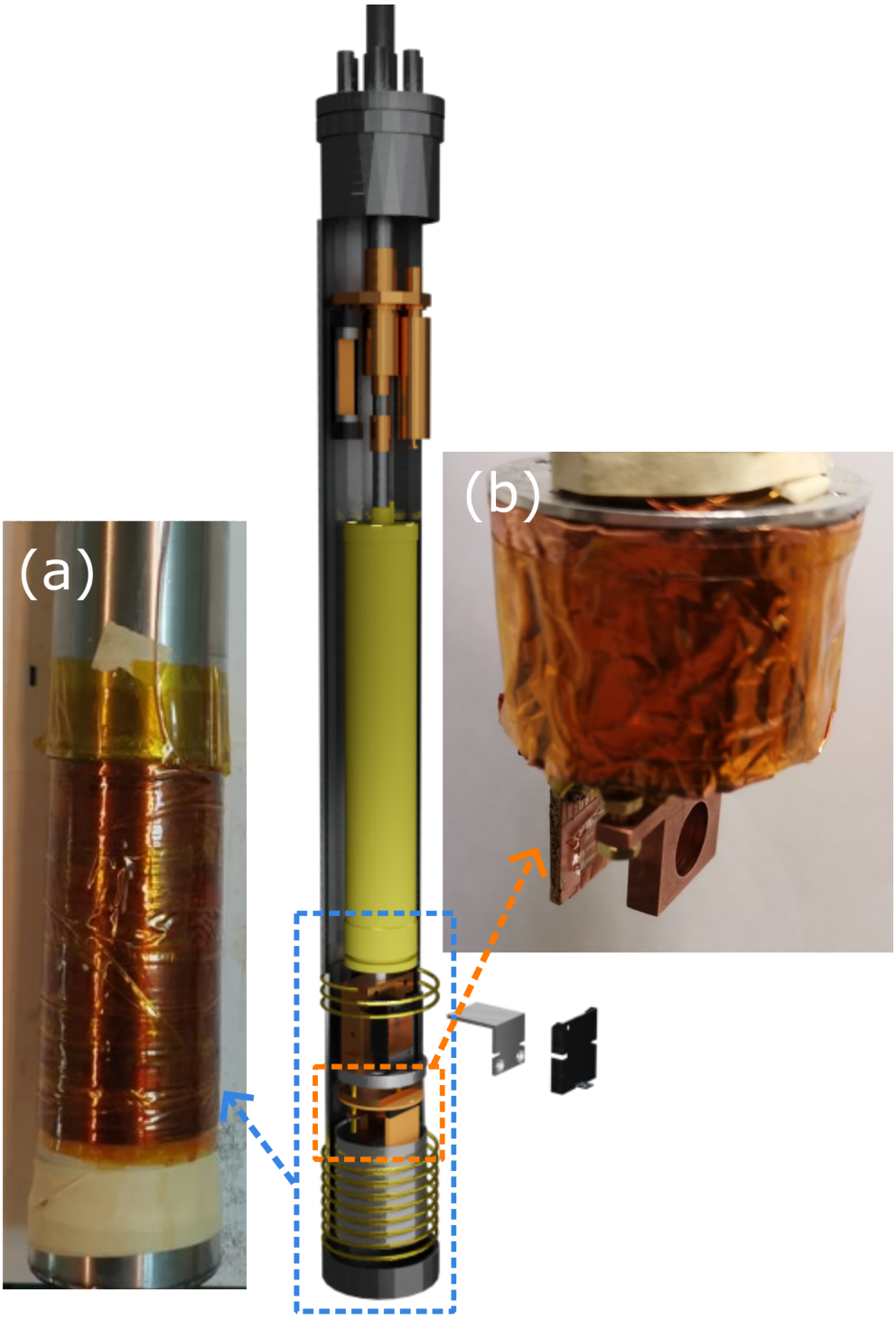

Figure 6: The schematic of the latest implementation of the low-temperature stages for the SFTED experiment. Panel (a) shows the modified and vastly improved implementation of the superconducting coil, and (b) the new sample stage design with the X-ray source mount.

This project has received funding from the European Union's Horizon 2020 research and innovation programme under grant agreement No 800923.

where higher statistics is required, i.e. to determine the energy resolution. Here we should note that the experimental results presented in this report have been exclusively measured with the lower activity source.

Although the activity of the X-ray source will diminish in time via radioactive decay, i.e. a Fe-55 source has a half-life of 2.737 years, leading to some uncertainty of the expected count rate, such information has a limited influence on the detector tests as long as pulses can be clearly resolved from the measurements.

We provide here an estimation of the expected X-ray count rate in the experiment.

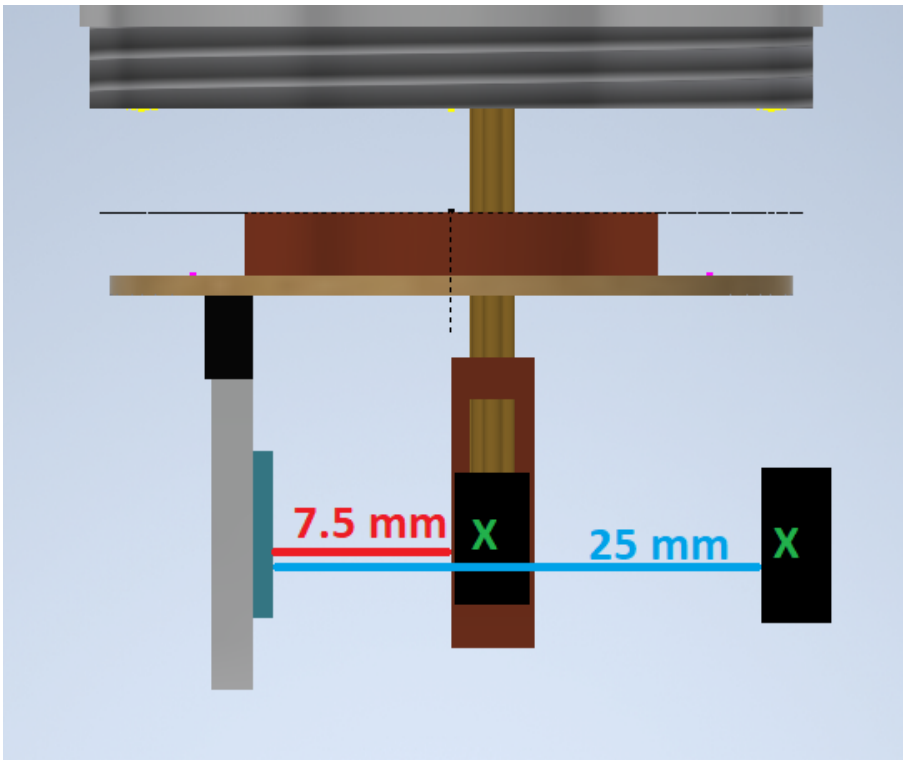

Figure 7: Illustration of the source mounting, having two options for distances (7.5 mm and 25 mm).

By the end of Feb.2023, the activity of the lower activity source is estimated to be 111 kBq. For the setup illustrated in Fig. 7, taking into account the 1 mm diameter initial collimation hole close to the source, the count rates at 100×100 μm^2 and 200×200 μm^2 absorbers, placed at the distance of 7.5 mm, are 1.5 Bq (counts per second) and 6 Bq, respectively. It should also be noted that the quantum efficiency (absorption probability) for the 350 nm thick Au and Sn absorbers to absorb a 5.9 keV photon are 0.26 and 0.13, respectively, which should be multiplied to the particle count rate to obtain the expected absorption rate. For example, we expect to observe X-ray events with the rate of 0.39 pulses per second (one event per 2.6 s) when using an 10^4 μm^2 Au absorber.

This project has received funding from the European Union's Horizon 2020 research and innovation programme under grant agreement No 800923.

5 Preliminary X-ray measurements

Currently, there are a total of six X-ray detection tests that have been carried out using three different types of devices. In this section, we present the results of these tests.

5.1 NIS detector

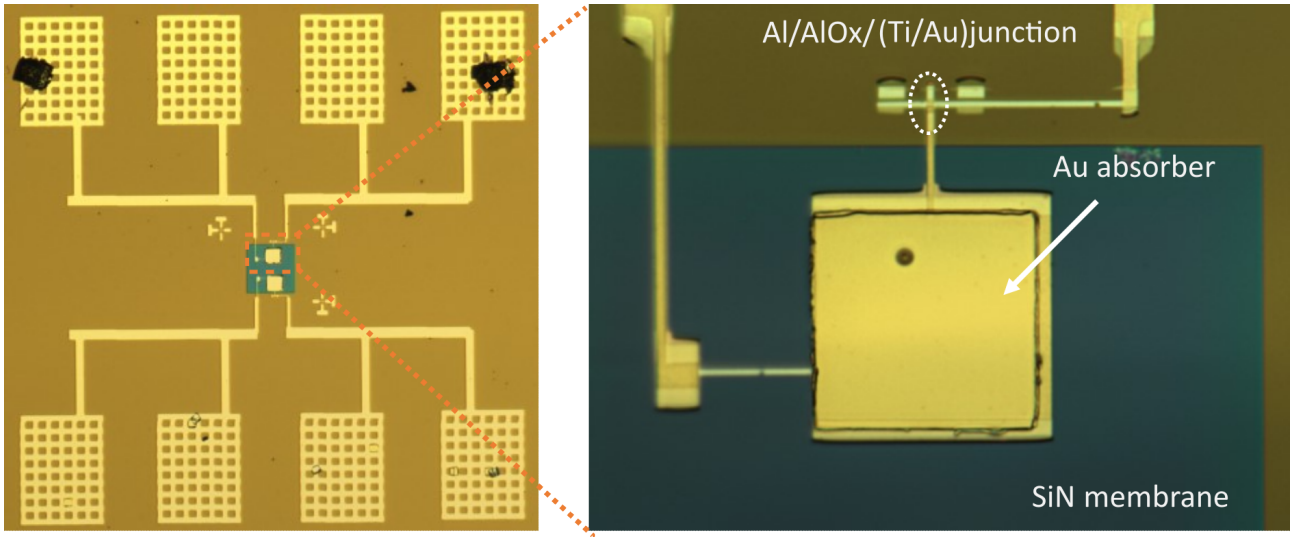

Figure 8: The optical microscope images of the tested NIS device.

The detector device we present first is a special sample, designated as NIS2201 (see Table 1 for all devices characterized at JYU), which was fully designed and fabricated at JYU for the SUPERTED project. The key components of this device are presented in optical microscope images in Fig. 8. A 350 nm thick Au absorber of size 100 μm $\times$ 100 μm lies on the top of a 500 nm thick suspended SiN membrane, and is electrically connected to a normal metal(Au)-insulator(AlOx)-superconductor(Al) (NIS) tunnel junction (area 0.6 μm$\times$0.8 μm) via a thin Ti/Au wire. Due to the lack of breaking of the electron-hole symmetry and spin polarization filtering in this device, it does not exhibit any thermoelectric response (ZT=0), and therefore it can only be used as an X-ray detector with an applied external bias [6]. (It still works based on the bolometric principle, measuring the temperature excursion caused by an X-ray absorption event.) However, there are several key similarities between the NIS X-ray detector and an SFTED detector, e.g. the tunneling barrier is AlOx for both (thus a NIS junction can be designed to have a similar R_T as an SFTED junction), the output signal is the tunnel current, and the required read-out system is identical. Therefore, a voltage-biased NIS device can be used as a good reference detector for comparison with an SFTED one, and it can serve as a test device to examine our X-ray source and read-out system built for the SFTED detector.

The measurement circuit setup and the measured dynamic conductance (dI/dV) of the device together with a theoretical fit are shown in Fig. 9. By numerically fitting the measured results to the well established NIS junction theory [7], the tunnel junction parameters were extracted as presented in Table 4.

In the X-ray detection test measurement, device NIS2201 was biased with 0.15 mV, and the output current signal was read out at a sampling rate of $\sim$ 540 kHz with a combined 120 samples per point averaging[1].

[1]Output signals were captured with a sampling rate of 540 kHz, and were recorded with an averaging of 60 samples per point (9 kHz). There is additional averaging of two samples per point in the numerical post processing.

This project has received funding from the European Union's Horizon 2020 research and innovation programme under grant agreement No 800923.

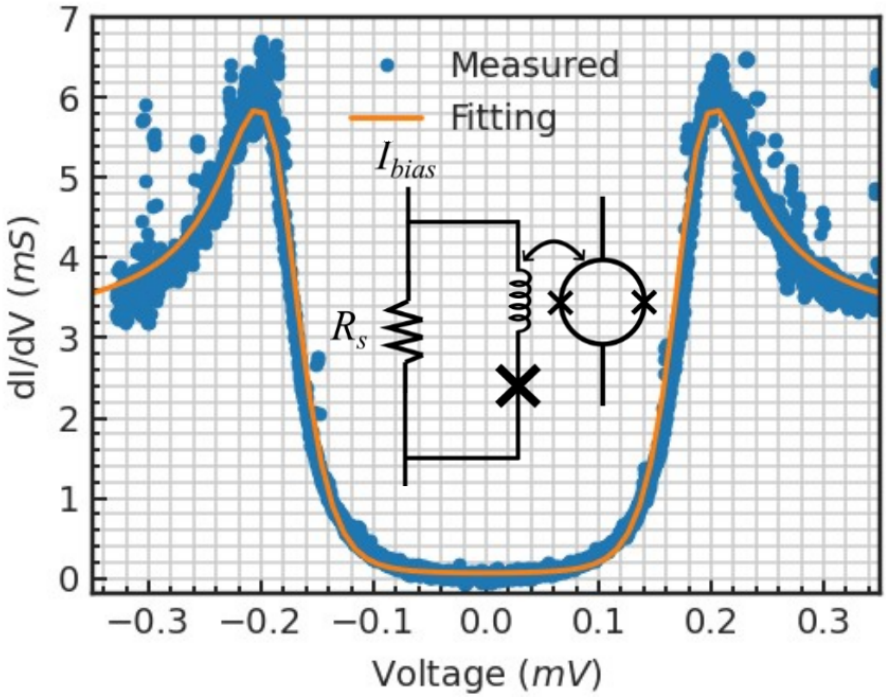

Figure 9: The voltage biased measurement circuit (R_s is the shunt resistor) and the measured dI/dV (at 0.25 K) of the NIS detector, with a theory fit.

Parameter	Result
Tunnel resistance R_T	330 Ω
Energy gap Δ_0	0.185 meV
Broadening Γ	$0.02\Delta_0$
Exchange field h	$0\Delta_0$
Polarization P	0

Table 4: Fitted parameters of NIS2201 device.

An example of a 50 s long output signal record is demonstrated in panel (a) of Fig. 10. Several prominent signal peaks over the general noise level can be seen from this record, and a zoomed view of a typical pulse is presented in panel (b). In panel (c), a typical record [2] is presented in the frequency domain. At frequencies above 100 Hz, above the roll-off of the pulse signal, the signal spectral density is ~ 2 pA/$\sqrt{Hz}$, slightly higher than the read-out noise reported in D3.2. We surmise that the excess noise originates from the external bias and the system grounding.

There are a total of 1332 pulse events recorded from the NIS2201 detector and these records were analyzed following the procedures and algorithms described in Ref. [8] which is a standard protocol for the analysis of modern transition edge sensor (TES) X-ray detectors. In panel (a) of Fig. 11, the recorded pulses are presented as functions of their peak current signal and pulse decay time. By omitting the outlier events (blue dots) from the graph, a model pulse is obtained as shown in panel (b), which is the average of all the remaining events (orange dots) in panel (a). Such model pulse represents the expected pulse shape of the detector, and has a peak signal of 0.08 nA and a pulse decay time slightly below 0.1 s. The ratio between the peak of the pulse and the general noise floor is relatively poor [see panel (a) of Fig. 10]. This is

[2] A record typically contains $\sim 6 \times 10^6$ data points. It corresponds to a 600 s record length if the recording rate is set to 9 kHz. In later experiments, different recording rates have been tested up to 50 kHz, i.e. an averaging of 12 samples per points was applied, corresponding to a 120 s record for each set.

This project has received funding from the European Union's Horizon 2020 research and innovation programme under grant agreement No 800923.

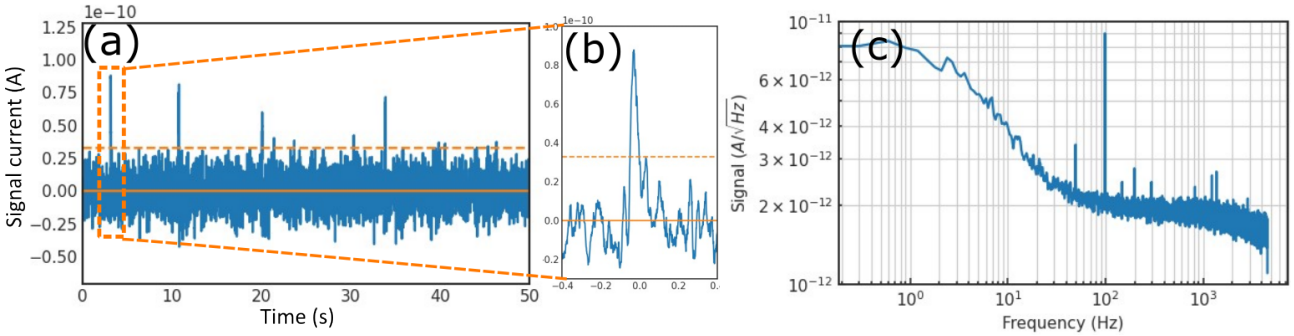

Figure 10: (a) An example of the SQUID output time series recorded from device NIS2201. (b) A zoom-in of a detected X-ray pulse from the data in (a). (c) The output signal presented in frequency domain.

likely due to the larger than optimal tunnel resistance ($R_T = 330\ \Omega$) and possibly larger than anticipated heat capacity of the Au absorber at 0.25 K, both of which reduce the temperature excursion.

Based on the extracted device parameters (Table 4) presented previously, we also computed the expected pulse shape numerically using a time-domain pulse shape simulation developed from our recent work on time-domain formulation of the SFTED response [9]. The result is shown in panel (c) of Fig. 11. The time constant of the simulated pulse is about the same as in the measurement, however, the computed pulse peak is about 4 times higher than in the measured pulse.

Two main channels contribute to the heat transfer in the device NIS2201, the electronic heat transfer via the tunnel junction, and the phononic heat flow escaping via the membrane to the substrate. In the computation we only included the first mechanism, heat transfer of the junction, which reproduces the relatively slow thermal time constant, as shown in panel (c). However the above mentioned assumption is not fully justifiable based on the experience with TES detectors, since in similar membrane isolated TES devices the thermal time constant is of the order of several milliseconds, set by the phonon thermal conductance. Such a discrepancy requires more studies to be understood.

5.2 Al/AlOx/Co X-ray test devices

X-ray detection tests were carried out with two Al/AlOx/Co devices (SF2209_dev1, SF2209_dev2, see Table 1 for full list of devices). The major goal of these devices was to optimize the tunnel resistance R_T as discussed in the previous section. However, their tunnel junctions have almost an identical design to the junctions for an actual detector, except that they lack the EuS layer. Hence we have not only executed the detector fabrication (i.e. defined junctions, deposited connection wires and the heavy-metal absorber) with these devices to test and further develop the fabrication protocols, but also performed X-ray detection test measurements to examine the read-out system and measurement procedures.

Optical microscope images of completed devices are demonstrated in Fig. 12. $200 \times 200\ \mu\text{m}^2$ Au absorber was deposited on top of the the normal metal Co wire in device SF2209_dev1 as shown in panel (a), whereas the same size superconducting Sn absorber was deposited on the Al electrode in device SF2209_dev2, as shown in panel (b).

Similar to the previously presented NIS2201 device, these two devices have no thermoelectric response due to the lack of the EuS layer, and thereby we have carried out the X-ray detection measurement with the biased circuit identical to that used with NIS2201 shown in Fig. 9. After the analysis of the experimental results, we came to the conclusion that the signals from the

This project has received funding from the European Union's Horizon 2020 research and innovation programme under grant agreement No 800923.

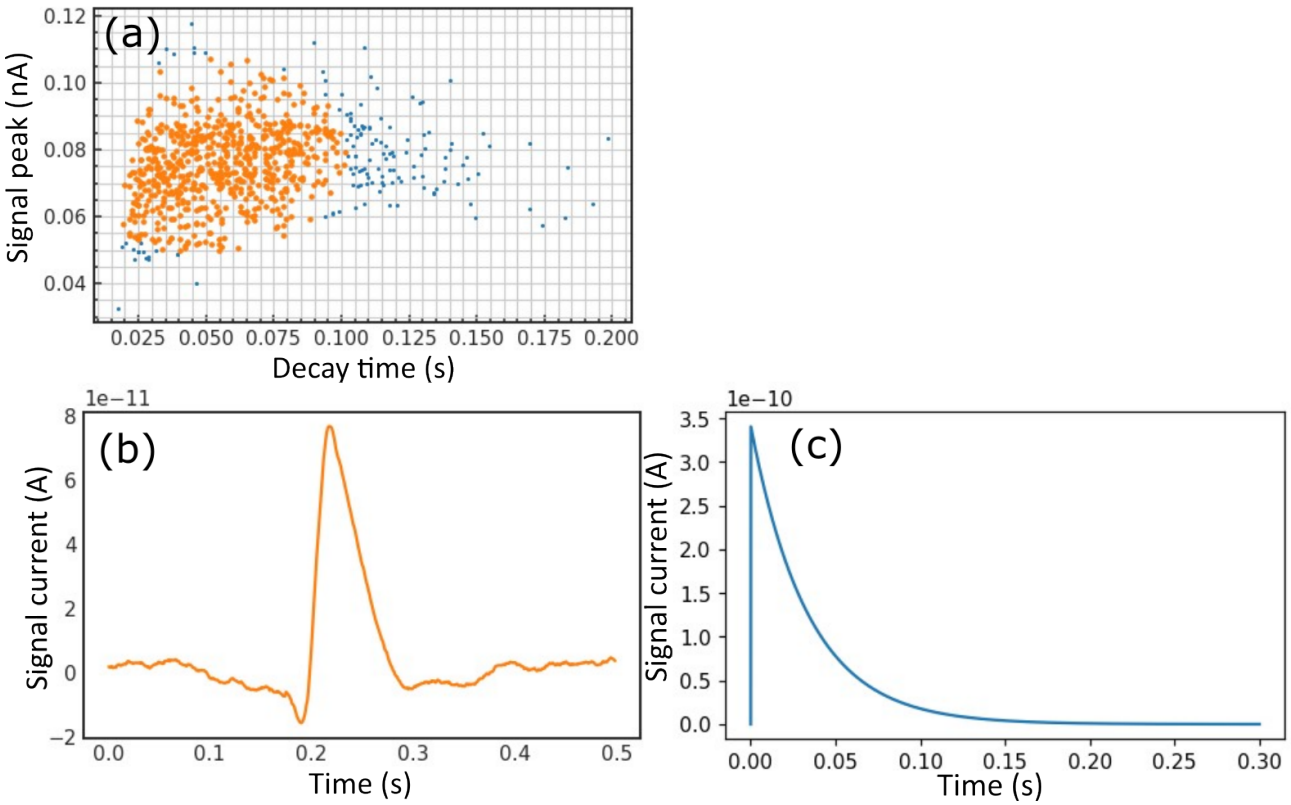

Figure 11: (a) Scatter plot of pulse events as functions of the peak of the pulse signal and the pulse decay time. (b) A numerical average of all recorded pulses except few outliers. (c) A computed pulse shape based on the extracted device parameters and an assumption that the junction thermal conductance is dominating.

pulse events were indistinguishable from the background noise in these devices. Examples of 50 s long signal records are demonstrated in Fig. 13, from device SF2209_dev1 in panel (a), and from device SF2209_dev2 in panel (b). The signal-to-noise ratio is too poor so that no pulse events can be identified. In addition, the recorded data are also presented in frequency domain, as shown in panels (c) and (d) for the two devices respectively. From the frequency spactra, we confirmed that the noise in these experiments was at a similar level as that from the reference device NIS2201.

Considering that the device SF2209_dev1 (2 hours oxidation, see Fig. 3) has an $R_T = 4.8$ kΩ and that device SF2209_dev2 (2.5 hours oxidation) has an $R_T = 8.2$ kΩ, their output current signals are estimated to be at least one order of magnitude smaller than that from the NIS detector NIS2201 ($R_T = 0.33$ kΩ). As a result, the above presented lack of pulses are expected. Nevertheless, these devices have been a great help to our development and optimization of the fabrication protocols and measurement procedures, influencing the project positively.

This project has received funding from the European Union's Horizon 2020 research and innovation programme under grant agreement No 800923.

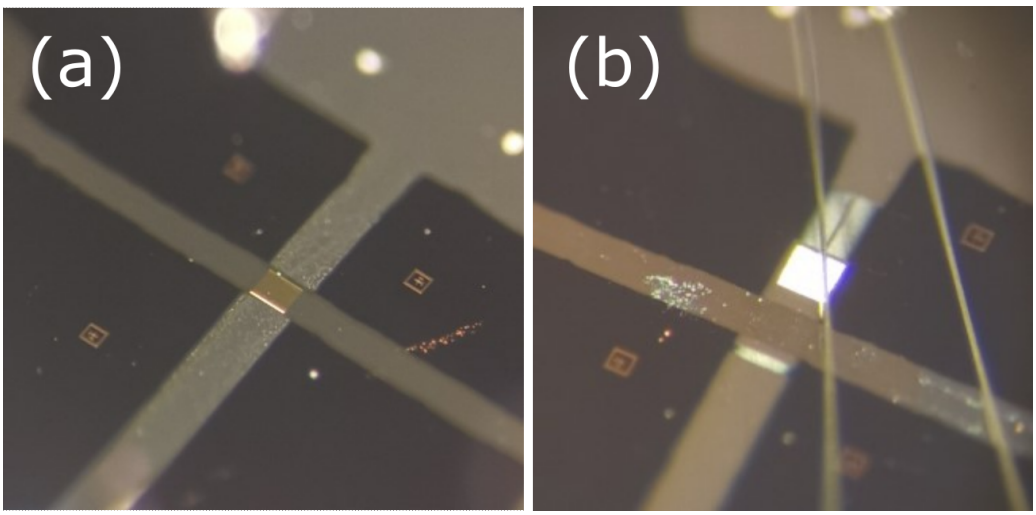

Figure 12: Optical microscope image of (a) SF2209_dev1 with Au absorber and (b) SF2209_dev2 with Sn absorber.

5.3 EuS/Al/AlOx/Co X-ray detectors

By the time of the writing of this report, the complete (EuS/Al/AlOx/Co) detector sample is in preparation, and we have not gathered enough data to report the results here.

6 Conclusions and outlook

In summary, to fulfill out task of realizing and demonstrating the first X-ray detector based on the giant thermoelectric effect in S/FI heterostructure, we have carried out more than 40 cryogenic experiments with 22 devices. The results of these measurements have been used to optimize and improve the design and fabrication protocol of the detector, as well as the design and implementation of the read-out and measurement setup. In this report, the preliminary X-ray detection tests have also been presented, however these tests have been executed with the externally biased reference devices (lack of EuS layer). These results suggest that with the optimized tunnel resistance of the device, X-ray pulse signals should be detected by a a more optimized detector device. An experiment with a complete SFTED device is in preparation, first in line in our future measurements.

This project has received funding from the European Union's Horizon 2020 research and innovation programme under grant agreement No 800923.

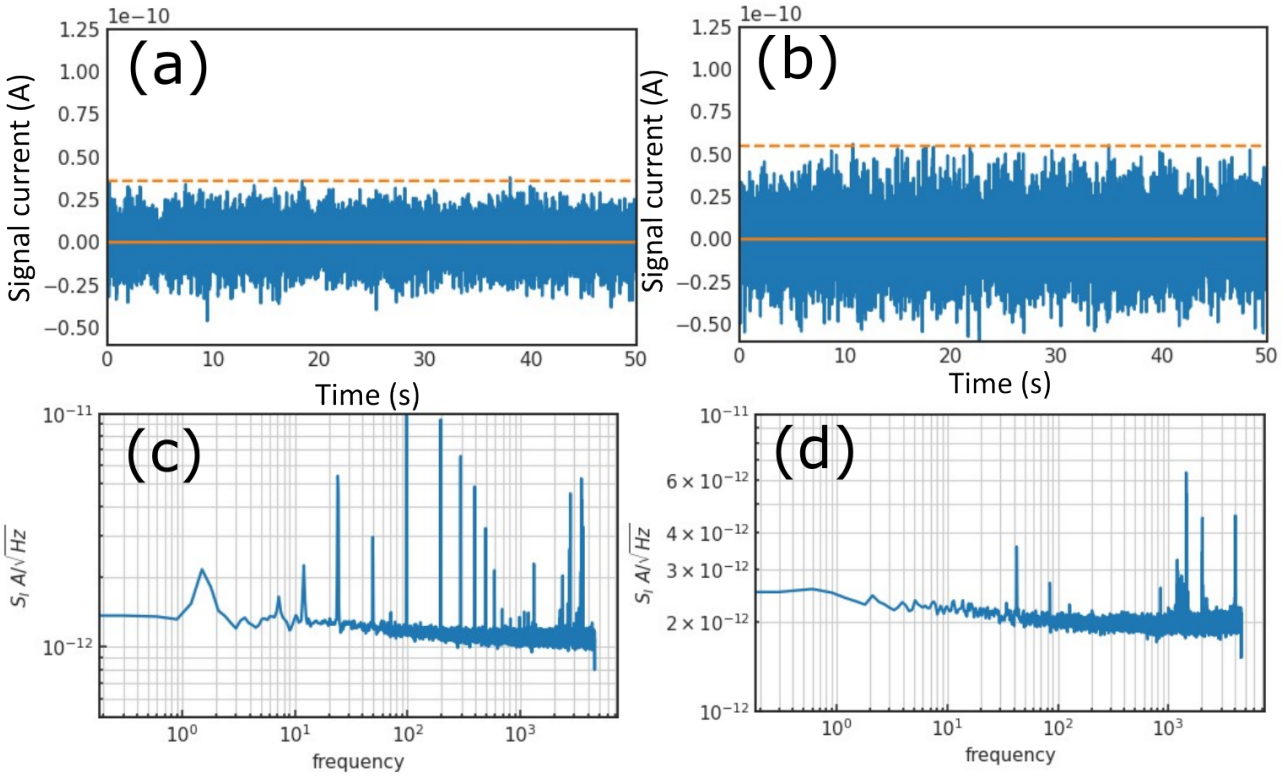

Figure 13: Clips of output signals recorded from devices (a) SF2209_dev1 and (b) SF2209_dev2. The output signals are presented in frequency domain for devices (c) SF2209_dev1 and (d) SF2209_dev2.

References

[1] Heikkilä T T, Ojajärvi R, Maasilta I J, Strambini E, Giazotto F and Bergeret F S 2018 *Phys. Rev. Appl.* **10** 034053 ISSN 23317019 (*Preprint* 1709.08856)

[2] Chakraborty S and Heikkilä T T 2018-09-28 *J. Appl. Phys.* **124** 123902 ISSN 10897550

[3] Geng Z, Helenius A P, Heikkilä T T and Maasilta I J 2020 *J. Low Temp. Phys.* **199** 585–592 ISSN 0022-2291, 1573-7357

[4] Ozaeta A, Virtanen P, Bergeret F S and Heikkilä T T 2014 *Phys. Rev. Lett.* **112** 057001 ISSN 00319007 (*Preprint* 24580623)

[5] Heikkilä T T, Silaev M, Virtanen P and Bergeret F S 2019-08-21 *Prog. Surf. Sci.* **94** 100540 ISSN 00796816 (*Preprint* 1902.09297)

[6] Nahum M and Martinis J M 1995 *Appl. Phys. Lett.* **66** 1478 ISSN 00036951

[7] Giazotto F, Heikkilä T T, Luukanen A, Savin A M and Pekola J P 2006 *Rev. Mod. Phys.* **78**(1) 217–274 URL https://link.aps.org/doi/10.1103/RevModPhys.78.217

[8] Fowler J W, Alpert B K, Doriese W B, Joe Y I, O'Neil G C, Ullom J N and Swetz D S 2016 *J. Low Temp. Phys.* **184** 374–381 ISSN 0022-2291 (*Preprint* 1511.03950)

[9] Geng Z and Maasilta I J 2022 *J. Low Temp. Phys.* **209** 419–426 ISSN 0022-2291, 1573-7357

This project has received funding from the European Union's Horizon 2020 research and innovation programme under grant agreement No 800923.